CEAS Space Journal
https://doi.org/10.1007/s12567-024-00556-w

ORIGINAL PAPER

Shock–shock interaction on the Reusability Flight Experiment (ReFEx)

Divek Surujhlal[1] · **Viola Wartemann**[2] · **Alexander Wagner**[1]

Received: 26 January 2024 / Revised: 2 May 2024 / Accepted: 24 May 2024

Abstract
The Reusability Flight Experiment (ReFEx) is currently under development at the German Aerospace Center (DLR). A coupled experimental and numerical campaign was carried out to investigate the surface heating on the payload geometry during return consisting of a forebody and canard. In this way, numerical tools for a post-flight analysis can be preemptively improved where required. Experiments were undertaken at the High Enthalpy Shock Tunnel Göttingen (HEG) on a 1:4 scale model with the use of temperature sensitive paint on the payload geometry to obtain surface heat flux. The model configuration was varied in angle of attack and canard deflection. Laminar and turbulence-model solvers in the DLR-TAU code were used for the numerical simulations. This investigation focussed on the shock–shock interaction of the nose bow shock with the leading-edge shock of the canards showing significant surface heat flux along the canard. Larger surface heat fluxes were measured in the experiments downstream of the shock interaction on the canard, than obtained from the laminar CFD calculations. This was attributed to transition of the boundary layer within the interaction regions, in the presence of significant adverse pressure gradients. Other flow features along the forebody in the vicinity of the canard were qualitatively matched better by the fully-turbulent numerical solutions than the laminar ones. This work aims to demonstrate the extent to which the numerical and experimental tools assist useful insights into flow phenomena during the return stages of the ReFEx payload geometry, and the aspects for which improvements are required.

Keywords Shock–shock interaction · Heat flux · Aerothermodynamics · Flight experiment · Temperature sensitive paint

1 Introduction

The Reusability Flight Experiment (ReFEx) is intended to demonstrate aerodynamic control in the return phase of the trajectory of a reusable launch vehicle (RLV). An aerodynamic controlled RLV offers an alternative to propulsive return, as indicated by preliminary studies by the German Aerospace Center (DLR) [1, 2]. The ReFEx RLV comprises the first stage of a 3-stage vehicle, with a two-stage booster configuration. Given that cost-intensive payloads are foreseen to be packaged into the first stage, safe return of this stage is of paramount importance. A schematic of the first stage of the ReFEx vehicle is shown in Fig. 1.

There are currently two main methods for controlled return of first stage payloads [4]. With vertical-takeoff-vertical-landing (VTVL), the payload is controlled during its return with a propulsion system. The development of a VTVL demonstrator is currently allocated to the scope of the CALLISTO Project within the DLR, CNES and JAXA Consortium. The second method is based on vertical-take-off-horizontal-landing (VTHL) and is the subject of the ReFEx project. In this way, DLR is able to build scientific and technical expertise in the development and flight testing of both types of RLVs.

During the return phase of the flight experiment the first stage will be subject to a hypersonic freestream and is required to decelerate in a controlled manner to landing.

Viola Wartemann and Alexander Wagner have contributed equally to this work.

✉ Divek Surujhlal
divek.surujhlal@dlr.de

Viola Wartemann
viola.wartemann@dlr.de

Alexander Wagner
alexander.wagner@dlr.de

[1] Spacecraft Department, Institute for Aerodynamics and Flow Technology, German Aerospace Center (DLR), Bunsenstraße 10, Göttingen 37073, Germany

[2] Spacecraft Department, Institute for Aerodynamics and Flow Technology, German Aerospace Center (DLR), Lilenthalplatz 7, 38108 Braunschweig, Germany

Published online: 10 June 2024

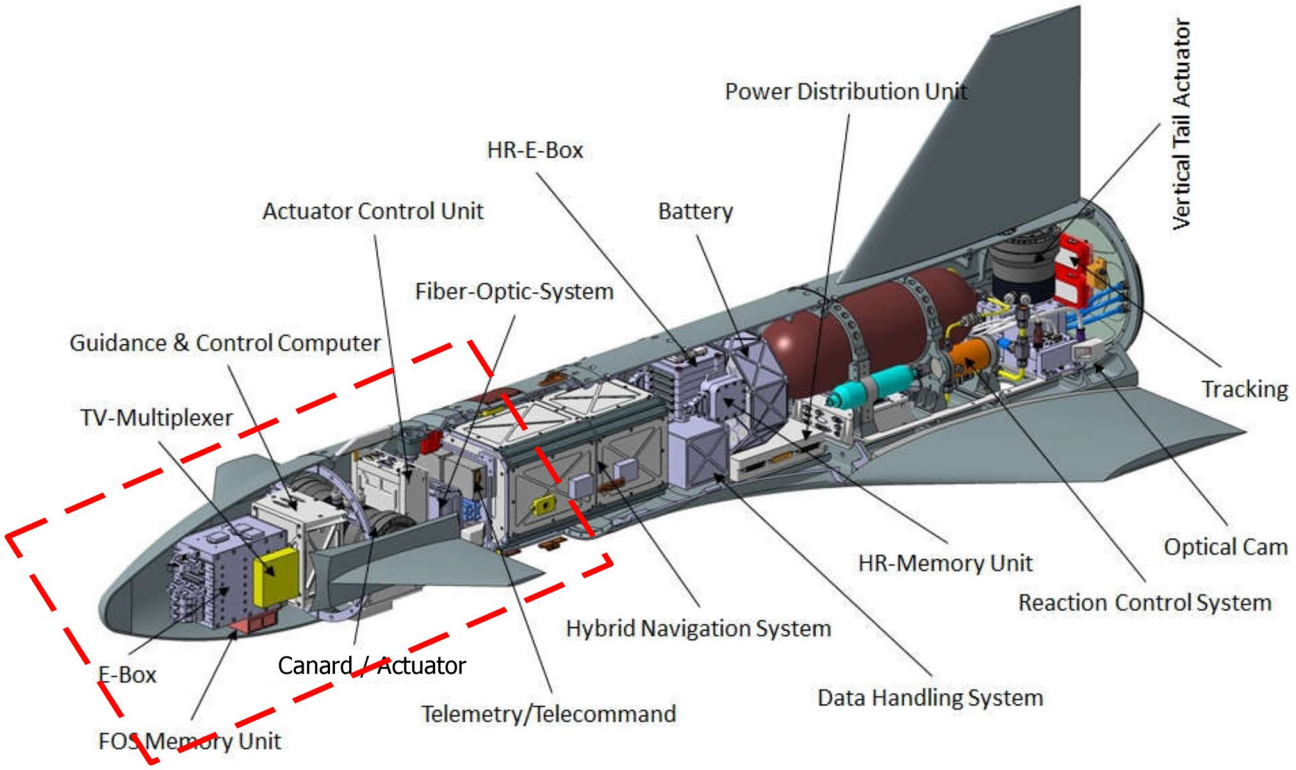

Fig. 1 System overview of the ReFEx first stage as detailed by Bauer et al. [3]. The payload section is located at the forward portion of the vehicle

This requires control surfaces (canards, see Fig. 1) on the forebody of the first stage. It is required to understand the aerothermodynamic loads on the forebody and canards during high-speed return.

This work presents a joint experimental and numerical study that was conducted for further insight into the aerothermal loads at various configurations relevant to the return phase of the ReFEx trajectory. Experiments were conducted on a 1:4 scale model with the intention to assist numerical re-building and specifically the prediction of flight vehicle heat loads. Such numerical models are foreseen for post-flight analyses.

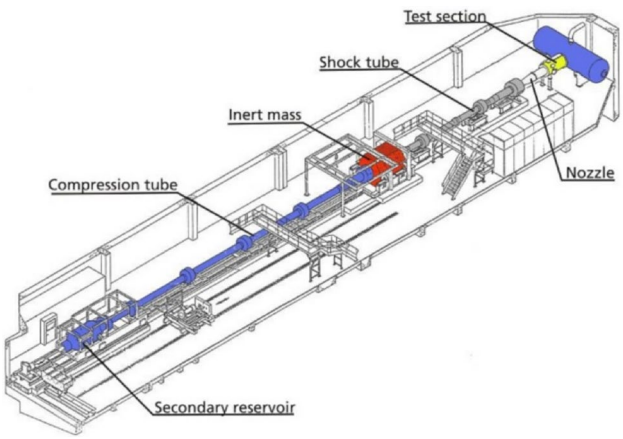

Fig. 2 Schematic overview of the HEG with main subsystems labelled

2 Experimental details

2.1 High Enthalpy Shock Tunnel Göttingen (HEG)

The High Enthalpy Shock Tunnel Göttingen (HEG) was allocated for experimental testing of the ReFEx payload section. The HEG is a free-piston-driven shock tunnel and was commissioned for the simulation of hypersonic freestream conditions relevant to reentry conditions. More information on the HEG has been published by the DLR [5]. A schematic overview of the HEG is shown in Fig. 2.

In this work, results will be presented based on tests conducted in freestream conditions representative of atmospheric reentry up to 30 km altitude at Mach 7.4 with a stagnation specific enthalpy of approximately 3.0 MJ/kg. This condition is shown in relation to an amalgamated return corridor [2] in Fig. 3. The location of the chosen

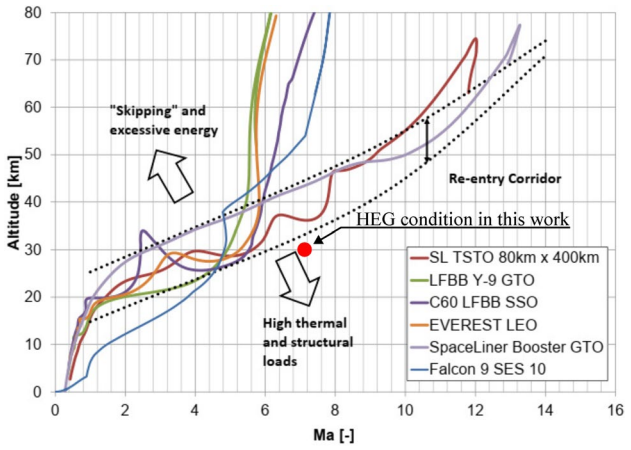

Fig. 3 An amalgamated reentry corridor [2] including the test condition used in this work

test condition in relation to the return corridor is due to the currently available set of test conditions of the HEG.

While the chosen HEG test condition does not represent a specific point on the ReFEx trajectory, the physical insights gained and modelling techniques used are expected to apply qualitatively to ReFEx trajectory points at a lower Mach number. Table 1 presents relevant reservoir and freestream parameters for the condition used in this work.

2.2 ReFEx test model geometry

The experiments at the HEG were focused on the ReFEx payload forebody and its control surfaces (canards). This geometry is indicated within the dotted box in Fig. 1. The objective was to quantify the surface heating loads experienced by the forebody during various configurations of the payload during flight. This meant that angles of attack, canard deflections and roll configurations (belly-up and belly-down) had to be considered. A subset of the results available to date are presented in this work.

The test model used for HEG experiments was a 1:4 scale model. Temperature sensitive paint (TSP) was the main diagnostic used from which surface heat flux on the forebody and a single canard was measured. A limited number of thermocouples (Type E, coaxial) and pressure transducers were placed on the model. These are indicated in Fig. 4.

Furthermore, the forebody was divided into two parts, one on which the instrumentation was installed (the green part in Fig. 4) and the surface onto which the TSP was applied, which included the canard. To replicate the flight geometry accurately, flight instrumentation ports and canard mounting structures were included in the test model and scaled accordingly from the flight geometry. A structural analysis was performed during the model design process to ensure that it would withstand the aerodynamic loads during a test in the HEG. Observations of reference markers on the model with the cameras from the temperature sensitive paint system (see below), showed the model to undergo no deformation or translation along the streamwise direction during the steady test time. No unexpected changes to the model geometry were observed during the tests at the HEG.

Table 1 Selected nominal operating conditions of HEG at $M = 7.4$

Condition	A
p_0 (MPa)	28.4
T_0 (K)	2582
h_0 (MJ/kg)	3.0
M_∞ (–)	7.4
T_∞ (K)	248
ρ_∞ (g/m^3)	43.2
u_∞ (m/s)	2350
$\mathrm{Re_m}$ (1/m)	6.4×10^6

2.3 TSP and optical system

The base layer for the TSP was coated onto the model surface and machined to the model contour. The TSP was then applied to the base layer for each test. An important consideration of TSP coatings is that the base layer acts as an insulator to the model surface [6]. The base layer thickness

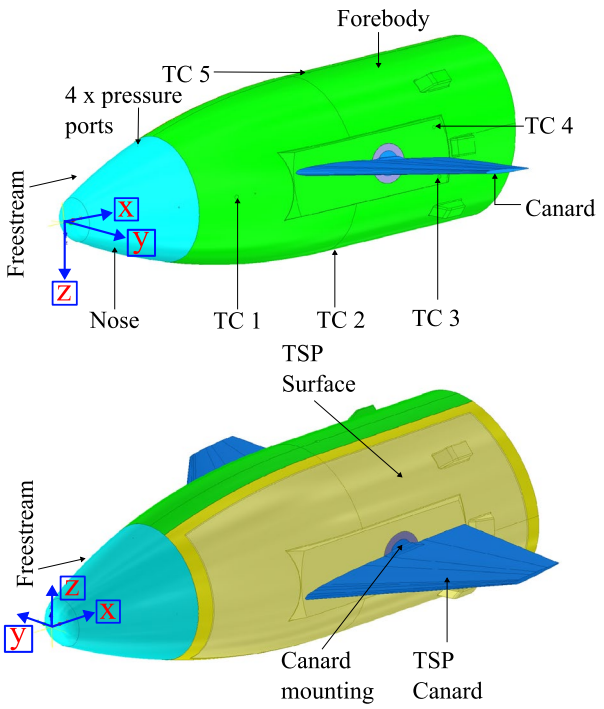

Fig. 4 Overview of instrumentation and key features of the ReFEx forebody geometry. The left- and right- hand sides of the model are shown. Thermocouple positions are indicated by "TC"

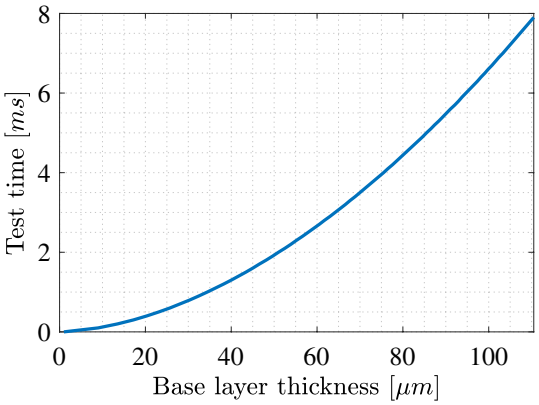

Fig. 5 Thermal penetration depth chart showing possible base layer thickness for a temperature change of Δ T = 1 K at the lower side of the base layer at the end of the test time for a constant heat flux of 2.0 MW/m^2

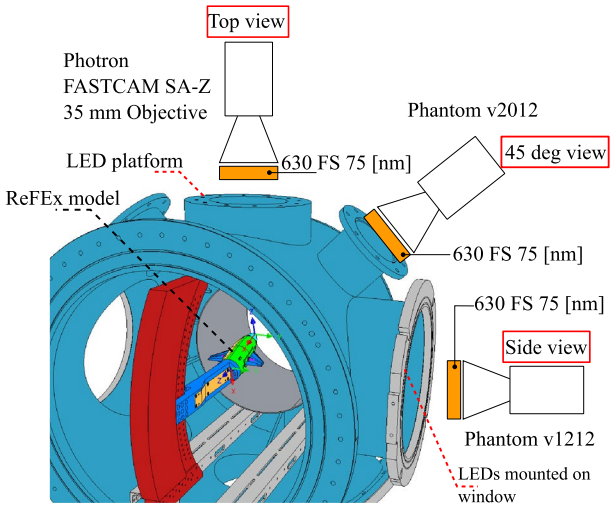

Fig. 6 Overview of optical setup for image acquisition of TSP emission. Three high-speed cameras were mounted around the test section of HEG

was targeted to be 100 µm and this was confirmed based on measurements along the model and canard. Figure 5 shows that, for the chosen base layer thickness, conduction of heat flux through to the model surface would happen after 7 ms, and therefore, after the tunnel test time. TSP composition development [6, 7] and time response calibration [8–10] informed the post-processing routines developed for the TSP results in this work.

Given the complex three-dimensional ReFEx geometry, multiple cameras were set up around the HEG test section to capture the emission from the TSP surface at different angles. This meant that the model geometry can be three-dimensionally reconstructed and facilitate further comparison with results from three-dimensional TAU computations [11]. The setup of the cameras in relation to the test section and model is shown in Fig. 6.

Surface heat-flux measurements were obtained from a temporal integration scheme of the temperature history for each pixel imaged from the measurement surface [12]. An in-situ calibration of the base layer following the procedures as detailed by Schramm et al. [6] and Ozawa et al. [7] was carried out. The base layer properties contained in the term $\rho_b c_b k_b$ was estimated for each camera system individually and was obtained to be 1035 J/m^2 K s$^{1/2}$ for the top camera. The base layer property estimations were iteratively solved to within ± 32 J/m^2 K s$^{1/2}$ and the estimated uncertainty in the derived heat-flux was 5% [7].

3 Numerical modelling

The numerical results presented in this paper are all based on the DLR flow solver TAU, which is a three-dimensional parallel hybrid multigrid code. The DLR TAU code has been validated in detail over the last decades. Information about the validation of supersonic flow simulation with TAU can be found, for example, in Gerhold et al. [13], Melber et al. [14] and Schwamborn et al. [15]. For an extensive validation of the TAU solver for hypersonic flows, Reimann et al. [16] and Mack et al. [17] can be taken as references. In Mack et al. [17] the heat flux, which is the focus of the current paper, is highlighted in detail for the validation using diverse geometries as well as flight conditions. The methods applied in the TAU code and in general in CFD are based on the fundamental governing equations of fluid dynamics. The reader is referred to subject matter-specific text books, see for example Pope [18]. The following summary cites reference Jack et al. [19]: DLR TAU is a finite volume solver, which solves the unsteady Reynolds-averaged Navier–Stokes equations (RANS)

$$\frac{\partial}{\partial t}\int_V w\mathrm{d}V + \oint_\Omega F n \mathrm{d}\Omega = 0 \tag{1}$$

in each finite cell volume dV of the simulation domain V. In Eq. (1) w denotes the vector of conservative variables and F that of the fluxes over the cells surface Ω with the surface normal vector n. Furthermore, the relations

$$w = \begin{pmatrix} \varrho \\ \varrho v \\ \varrho E \end{pmatrix} \tag{2}$$

$$F = \begin{pmatrix} \varrho v \\ \varrho v \otimes v + pI \\ \varrho E v \end{pmatrix} - \begin{pmatrix} 0 \\ \sigma \\ \sigma v + \lambda \nabla T \end{pmatrix} \tag{3}$$

are given where ϱ is the density, v the velocity, E the energy and T the temperature of the fluid. The stress tensor σ is calculated from the local velocity gradients and the fluid's viscosity μ as follows:

$$\sigma = \mu(\nabla \otimes v + v \otimes \nabla) - \frac{2}{3}\mu(\nabla \cdot v)I. \tag{4}$$

The investigated test cases in this work were all conducted at a total enthalpy of approximately 3.0 MJ/kg (see Table 1), at which the gas can be assumed to be perfect. Thus the perfect gas model is used for which the following equations of state apply:

$$p = \varrho RT \tag{5}$$

$$E = c_p T + \frac{1}{2}(v \cdot v) \tag{6}$$

The viscosity of the fluid was modelled using

$$\mu = \mu_{\text{ref}} \frac{T_{\text{ref}} + C}{T + C} \left(\frac{T}{T_{\text{ref}}} \right)^{\frac{3}{2}} \tag{7}$$

which is the Sutherland equation. For the heat conduction

$$\lambda = \frac{\mu c_p}{\text{Pr}} \tag{8}$$

a constant Prandtl number Pr was used as shown in Eq. (8), wherein the specific heat capacity at constant pressure was defined as

$$c_p = R\frac{\gamma}{\gamma - 1}. \tag{9}$$

In this paper laminar and turbulent approaches for the boundary layer are applied. To enable simulations of turbulent flows without resolving all time- and length-scales, the Favre averaging of the primitive variable Φ is introduced, that decomposes its instantaneous local value into an averaged part $\widetilde{\Phi}$ and a fluctuating part Φ''.

$$\Phi = \widetilde{\Phi} + \Phi'' \tag{10}$$

$$\text{with} \quad \widetilde{\Phi} = \frac{\overline{\rho\Phi}}{\overline{\rho}} \tag{11}$$

$$\text{and} \quad \overline{\Phi}(x,t) = \lim_{N\to\infty} \frac{1}{N} \sum_{i=1}^{N} \Phi_i(x,t). \tag{12}$$

Introducing the described averaging into the system of conservation equations, the flux density vector is extended by the turbulent part F_{t}.

$$F_{\text{t}} = \begin{pmatrix} 0 \\ \sigma_{\text{t}} \\ \widetilde{v}\sigma_{\text{t}} - c_p \frac{\mu_{\text{t}}}{\text{Pr}_{\text{t}}} \nabla \widetilde{T} \end{pmatrix} \tag{13}$$

$$\text{with} \quad \overline{\rho}\sigma_{\text{t}} = \overline{\rho v'' \otimes v''} \tag{14}$$

$$\text{and} \quad \overline{\rho}\widetilde{k} = \frac{1}{2}\overline{\rho(v'' \cdot v'')} \tag{15}$$

$$\text{and} \quad \mu_{\text{t}} = \overline{\rho}\frac{\widetilde{k}}{\omega}. \tag{16}$$

Due to the short measurement times of the HEG, the model wall temperature for all test cases was assumed to be isothermal at 293 K which is termed a cold wall condition since the wall temperature is low relative to the stagnation temperature of the test gas. Hybrid grids, using tetrahedrons and prisms, with about 12 million points were applied. The grids are especially clustered towards the nose and the leading edges (see Fig. 7). The first layers of the boundary layer were arranged such that a linear temperature distribution from cell to cell was provided, beginning with the assumed cold wall.

During the ReFEx project various grid studies were performed, including the flight geometry grid as well as wind tunnel model grids. The grid studies were performed for the whole range of the planned trajectory with varied Mach numbers as well as angle of attacks (see for example Wartemann et al. [20]). The grid study for the applied meshes was performed with four different grids for the test case with AoA $\alpha = 0°$ and $\eta = 0°$. Two aspects are taken into account for the grid study: the aerodynamic coefficients as well as the heat flux. The aerodynamic coefficient C_x is summarized for the four different grids in Table 2. The medium grid and the final chosen grid delivers nearly the same value of this coefficient. Here the value of the coefficient C_x differs only by 0.3 %. Additionally the heat flux was investigated for the grid study, which is summarized in Fig. 8. For the final grid 4 the same contour colour distribution as for all main results

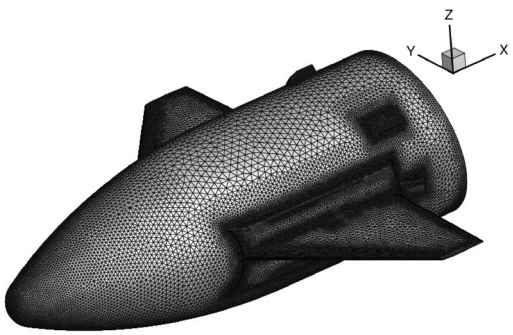

Fig. 7 Example of surface grid

Table 2 Grid study: aerodynamic coefficient C_x

Grid name	Grid points in millions	C_x	ΔC_x (%)
Coarse grid 1	2.1	− 0.295	3.5
Coarse grid 2	4.5	− 0.288	1.0
Medium grid 3	8.5	− 0.286	0.3
Final grid 4	12.0	− 0.285	–

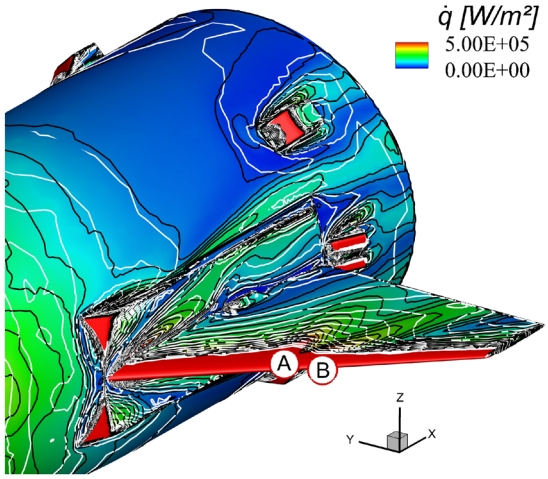

Fig. 8 Grid study: heat flux distribution

discussed in this paper was applied in Fig. 8. Further to this, the black contour lines illustrate the result for the medium grid 3, whereas the white contour lines mark the result for coarse grid 1. There are clearly visible differences between the contours for each of the grids, such as the definition of the structures A and B which were well-defined for the final grid 4 and which merged together for the coarse grid 1. Therefore, the finest mesh with 12 million grid points was chosen. Additionally, at two slides (near the positions A and B along the canard: $y = -0.073$m and $y = -0.081$m) a comparison of the heat flux for grid 1 and 3 in Fig. 9 is shown. Grid 1 and 3 are chosen to illustrated the differences, because between grid 3 and 4 no differences are visible along the chosen y-coordinates.

A constant turbulent Prandtl number $\mathrm{Pr_t}$ is used in all simulations with turbulent boundary layers. The one-equation Spalart–Allmaras model was chosen as a turbulence model [21]. A single model transport equation was solved for the turbulent viscosity. For a detailed description see, for example, Pope et al. [18]. The effect of the chosen turbulence model on calculations with the ReFEx geometry was investigated in Wartemann et al. [20], where different free stream conditions were analysed with various turbulence models. The highest detected difference between the models based on the aerodynamic coefficient C_x was about 2 %, and

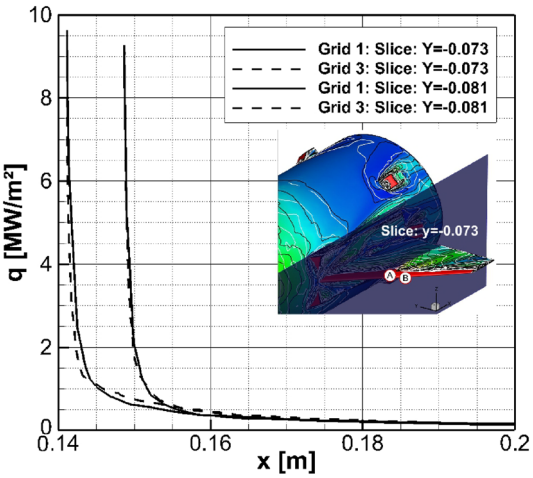

Fig. 9 Grid study: heat flux along $y = -0.073$m and $y = -0.081$m

for all other coefficients the differences were lower depending on the investigated free stream condition. Furthermore, the $k - \omega$ turbulence model was investigated revealing differences compared with the Spalart–Allmaras model. This comparison regarding the surface heat flux on a 0° canard is shown in Fig. 10. The features at the canard appear more defined for the Spalart–Allmaras model, as indicated by the two arrows in Fig. 10a. The contours are scaled to the same range as the experimental images. The better definition of the features on the canard surface which corresponded to the experimental images meant that the Spalart–Allmaras turbulence model was carried forward for all turbulence calculations.

4 Results

4.1 Calibrated surface heat flux

As described in Sect. 2.3, the proximity of the thermocouple TC 5 with the TSP surface on the forebody enabled an in-situ calibration of the base layer material properties, such that heat flux could be extracted from the TSP intensity images. The basis for this calibration was, therefore, the heat flux signal from the thermocouple. This is plotted in Fig. 11, also showing the mean and standard deviation bounds of the mean heat flux. To assess CFD validation of the surface heat flux, this was compared with the heat flux from the thermocouple, and is plotted in Fig. 11. The heat flux time signal from the thermocouple was filtered with a Savitzky–Golay filter with a window length of 101 samples and a polynomial of order 6. This shows that the CFD result somewhat underpredicted the mean heat flux measured by the thermocouple, but is within a single standard deviation of the mean. Surface heat flux extracted from the CFD solution

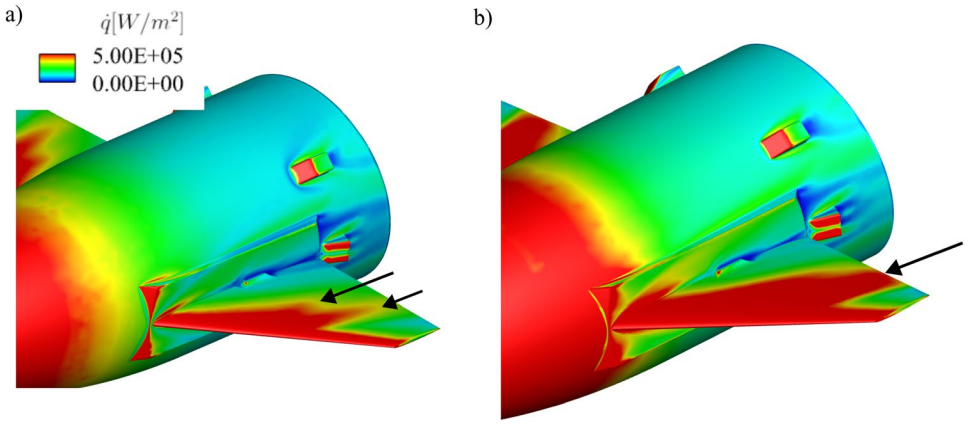

Fig. 10 Comparison of different turbulence models regarding surface heat flux. **a** Spalart–Allmaras model; **b** $k-\omega$ model

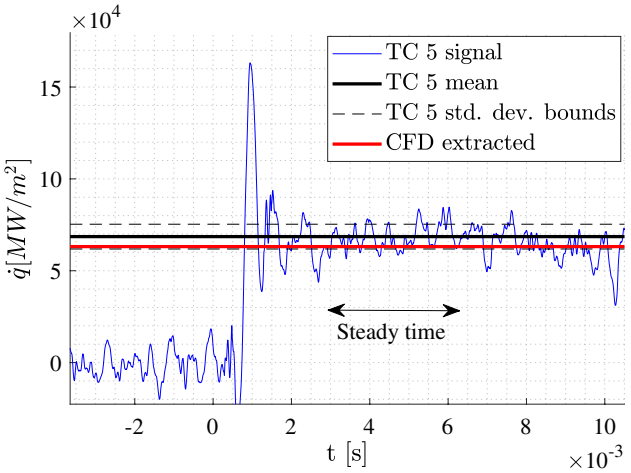

Fig. 11 Time signal of the thermocouple TC 5, filtered with a Savitzky–Golay filter with a window length of 101 samples and polynomial order 6. This used for heat flux calibration of the TSP diagnostic. Mean and signal standard deviation bounds for the heat flux are also shown, as well as the value extracted from the CFD solution. Model AoA was $\alpha = 0° \pm 0.01°$ with canards at $\eta = 0° \pm 0.01°$

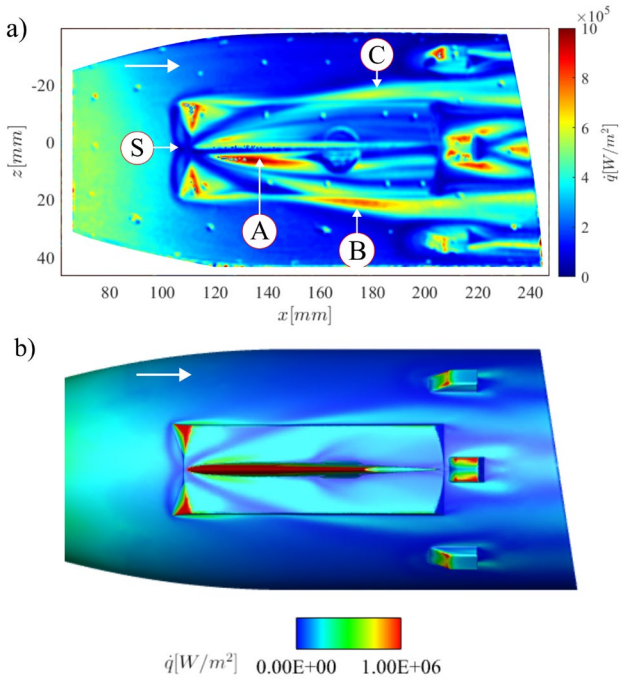

Fig. 12 Field comparison of mean heat flux as calculated from TSP (above) and from the CFD solution for a model AoA $\alpha = 0° \pm 0.01°$ with canards at $\eta = 0° \pm 0.01°$. Colour mappings are based on the same scales. Freestream flow is from left to right, as indicated by the arrows at the top left of each subfigure

was sampled at the same geometrical location on the body as the thermocouple. The locations were based on identical body-fixed coordinates, as shown in Fig. 4. A comparison of the heat flux field derived from the TSP with that extracted from the CFD solution is shown for the case with the model body angle of attack (AoA) $\alpha = 0°$ with canards at $\eta = 0°$ in Fig. 12. Here, the canard angle (η) is defined relative to the body angle (α).

Along the forebody, there is a significant reduction in the heat flux in the downstream direction, corresponding to the favourable pressure gradient on the forebody and the expansion of the flow. This is reproduced in the numerical results. Both results in Fig. 12 show multiple shock–shock and shock wave/boundary layer interactions (SWBLIs) occurring in the vicinity of the canard. The result from the experiment displays a slight asymmetry due to the angle of the canard being adjusted to within $\pm 0.01°$. An important difference is that the measured heat flux field in Fig. 12a shows significantly higher surface heat fluxes than the CFD result, in regions of reattachment of the flow on the forebody. These regions are marked A in Fig. 12a. Related investigations on shockwave/boundary layer interactions (SWBLI) by Wagner et al. and Sandham et al. [22, 23] confirmed that a transitioning boundary layer undergoing reattachment can result in a higher surface heat flux than during laminar reattachment. It is therefore expected that the larger measured

surface heat flux was due to a locally-transitional boundary layer. Boundary layer transition was not considered in the current CFD simulations.

It is also noteworthy that the reattachment of the flow outboard of the step on which the canard is mounted (marked B and C in Fig. 12a) is also a source of significant surface heat flux, which is again measured larger for the experiment than computed in the CFD result. A significant separation region is observed to exist upstream of the step mounting the canard and originating at the canard leading edge (marked S in Fig. 12a). This is well-described by the CFD result, matching the form of the separation region measured in the experiment. Overall, the CFD solutions were found to compare qualitatively well with the experimental results.

4.2 Overview of the shock–shock interaction at the canard

To obtain a broader impression of the flow around the ReFEx forebody, the 3-D field CFD solutions were examined, together with the different view perspectives obtained from different cameras mounted on the HEG test section (see Fig. 6).

A few main flow features are discussed pertaining to Fig. 12. In this section, particular examination is made of the shock–shock interaction at the canard. This interaction exists due to the nose bow shock interacting with the leading edge shock of the canard. An overview of this situation is shown in Fig. 13.

The pressure contours plotted on the z-plane show large pressure increases on the canard and it presents a critical location for examination of surface heat flux. The boundary layer development on the swept canard is impacted by large adverse pressure gradients, and the possibility of separation makes this a critical vehicle surface from an aerodynamic perspective.

The canard shock–shock interaction was examined in the context of Fig. 14. In Fig. 14a, a pressure isosurface (with $p = 20$ kPa) illustrates the bow shock generated at the nose of the forebody. This envelops the forebody, with supersonic flow downstream of the weak oblique portions of the shock. The supersonic flow downstream of the nose bow shock gives rise to a second shock generated at the leading edge of both canards. The two shocks (nose bow shock and canard leading edge shock) interact leading to intense heating on the canard surface. This is examined in Fig. 14b which is extracted from the laminar CFD solution. The mean heat flux measured from the TSP is shown in Fig. 14c. This is a top view of the forebody and canard.

The canard leading edge heating is evident due to the presence of the leading edge shock. The TSP molecules reached their excitation limit and this meant that there was no signal obtained at the regions of excessive surface heat

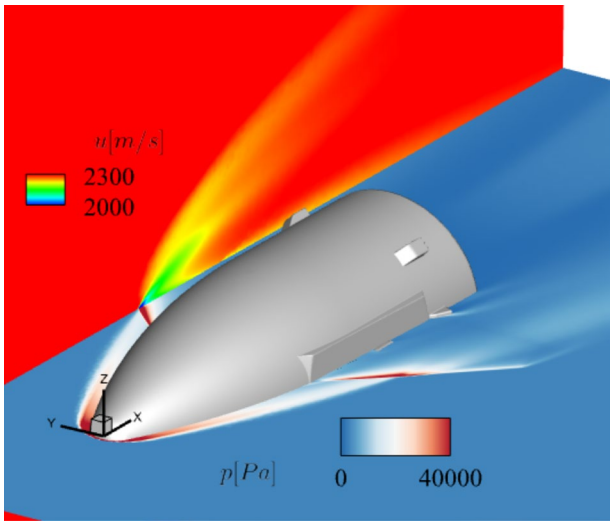

Fig. 13 Overview of the shock–shock interaction involving the nose bow shock with the leading edge shock at the canard. The z-plane shows contours of pressure. The y-plane shows contours of streamwise velocity. Model AoA $\alpha = 0°$, canard angle $\eta = 0°$

loads. The key features of the shock–shock interaction on the canard are labelled A, B and C. Feature A corresponds to the impingement of the nose bow shock with the canard leading edge shock. This results in intense heating in this region on the canard downstream of its leading edge. Due to the presence of this interaction, separation of the boundary layer is expected inboard of the shock impingement location at A. The resulting outboard reattachment of the boundary layer is labelled as feature B. This was confirmed by plotting the skin friction lines on the canard, as shown in Fig. 16. The divergence of the streamlines corresponds to the reattachment zone [24] and resulted in an increased surface heat flux. This was shown to persist for a longer distance in the streamwise direction for the TSP data obtained from the experiment at HEG than shown in the CFD result. This is attributed to the possible transition of the boundary layer on the canard resulting in higher momentum of the reattached flow and non-localised heating shown in the experiment. The reattaching flow on the canard interacts with the outboard flow downstream of the leading edge shock and the difference in momentum of these two regions results in the development of a vortex, labelled as C in Fig. 14b and c. Lower surface heating was predicted by the laminar CFD solution for the region C. Further proof of the existence of feature C corresponding to an outboard vortex is depicted in Fig. 15, showing an isosurface of streamwise vorticity ($\omega_x = 2 \times 10^6\ \mathrm{s}^{-1}$) on the canard. The isosurface is coloured by heat flux contours and illustrates that the feature observed as a reduced surface heat flux from the TSP image on the outboard region of the canard corresponds to an outboard vortex.

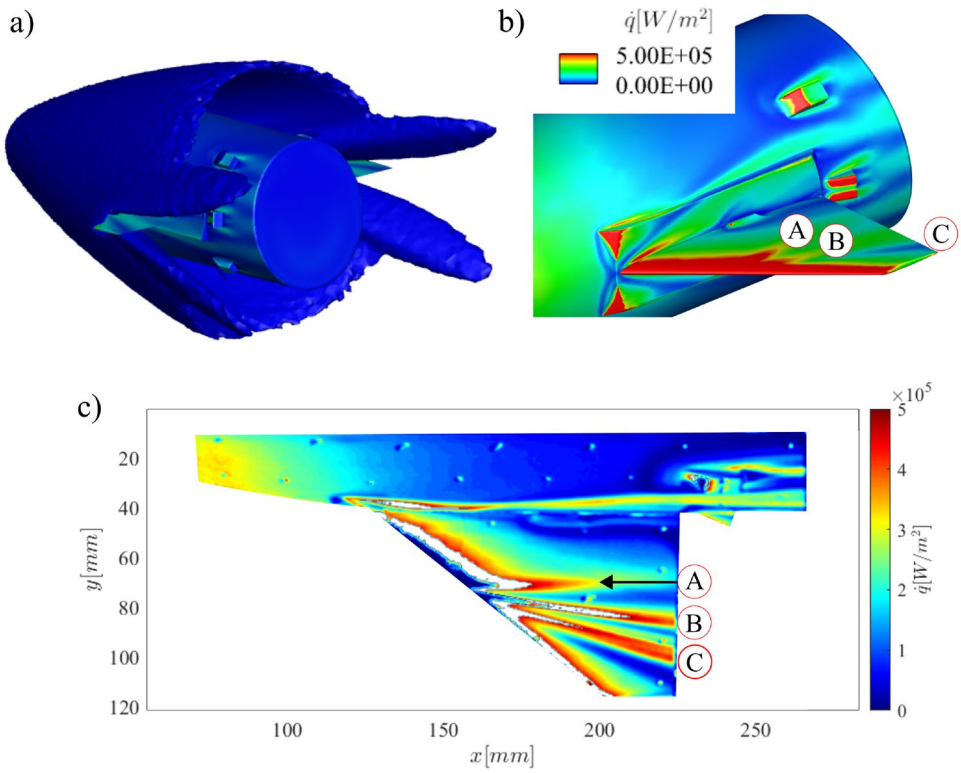

Fig. 14 Detailed view of the shock–shock interaction at the canard. **a** Isosurface of pressure ($p = 20$ kPa) illustrating the nose bow shock and its envelopment of the ReFEx forebody as well as the diffraction of the shock surface due to the shock–shock interaction with the canard; **b** surface contours of heat flux on the forebody; **c** heat flux contours derived from TSP data showing the ReFEx forebody as viewed from the top. Freestream flow is from left to right. Model AoA $\alpha = 0° \pm 0.01°$, canard angle $\eta = 0° \pm 0.01°$

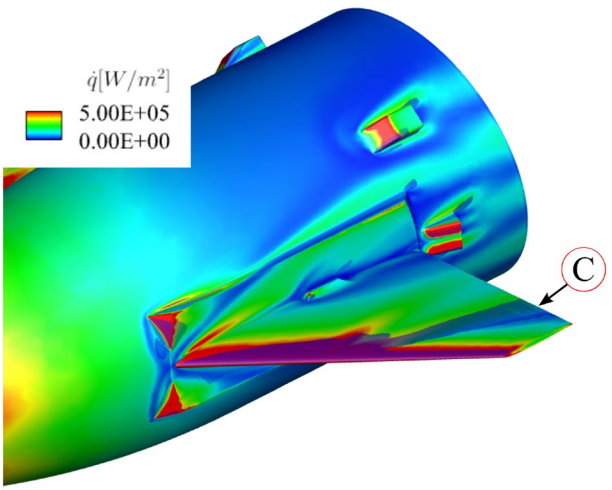

Fig. 15 View of the shock–shock interaction at the canard with an isosurface of streamwise vorticity ($\omega_x = 2 \times 10^6\ s^{-1}$) illustrating that the surface feature named denoted C observed from the TSP corresponds to an outboard vortex. The isosurface is shaded with contours of heat flux and is partially transparent for display purposes. Model AoA $\alpha = 0° \pm 0.01°$, canard angle $\eta = 0° \pm 0.01°$

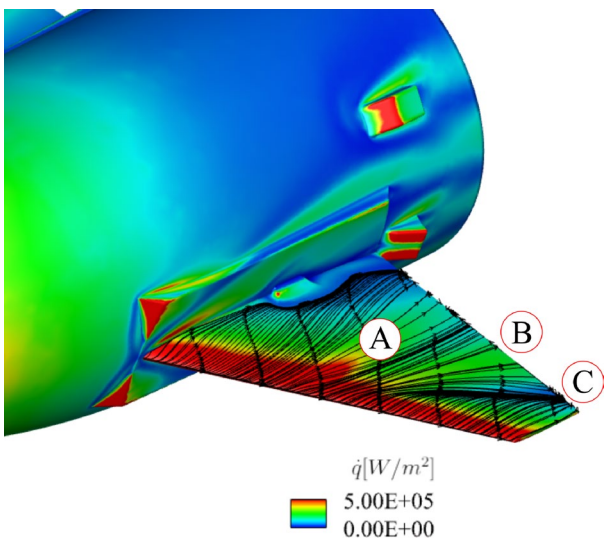

Fig. 16 Detailed view of the shock–shock interaction at the canard with lines of skin-friction at the surface of the canard superimposed on contours of surface heat flux. Model AoA $\alpha = 0°$, canard angle $\eta = 0°$

To investigate the possibility that the boundary layer along the canard transitions to turbulence due to the shock–shock interactions, a turbulent CFD calculation was carried out. The Spalart–Allmaras turbulence model was used with the same surface grid and with the ReFEx payload geometry configured with a model AoA $\alpha = 0°$ and canard angle $\eta = 0°$. The surface heat flux contours on the canard are shown in Fig. 17

The shock impingement location A results in a larger separation region indicated by the larger extent of the high surface heat flux region, compared with the laminar CFD

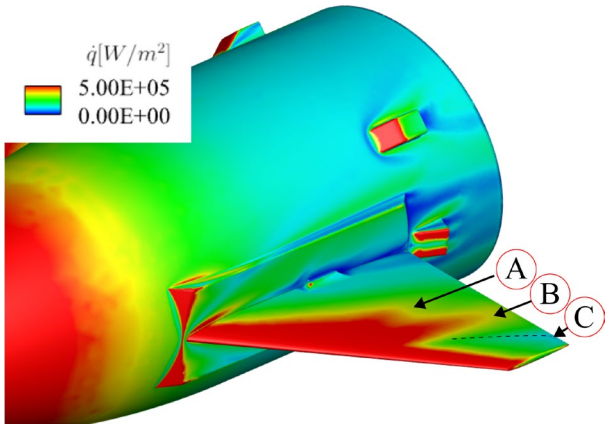

Fig. 17 Detailed view of the shock–shock interaction at the canard with surface contours of heat flux on the forebody and canard. Model AoA $\alpha = 0°$, canard angle $\eta = 0°$. The Spalart–Allmaras turbulence model was used in this case

solution. This is typical of hypersonic shockwave/turbulent boundary layer interactions [22, 24]. The reattachment vortex B also results in non-localised heating and is attributed to the higher momentum of the boundary layer compared to the laminar case. The outboard vortex C is notably weaker than with the laminar case, and could be explained by the generally higher momentum of the near-wall flow along all outboard regions of the canard, which acts to diffuse the roll-up of the vortex in this region.

The features A, B and C in Fig. 17 are not as distinctly demarcated as they are in the mean heat flux field obtained from the TSP image in Fig. 14. However, the fact that the features are non-localised in terms of surface heating is qualitatively captured by the turbulent solution. In the absence of a definitive conclusion on the status of the boundary layer along the canard, it is deemed satisfactory to use the laminar CFD solutions for further qualitative comparisons.

4.3 Shock–shock interaction with variation in model configuration

Examination of the shock–shock interaction at the canard was carried out for model configurations with:

- Model AoA $\alpha = 0°$, canard angle $\eta = 15°$
- Model AoA $\alpha = 17.17°$, canard angle $\eta = 0°$

Here, the canard angle (η) is defined relative to the body angle (α).

Mean surface heat flux contours derived from the TSP data are shown in Fig. 18. The nose bow shock impingement on the canard is labelled A in Fig. 18a, b. In both cases, the leeside of the canard surface is viewed, meaning that

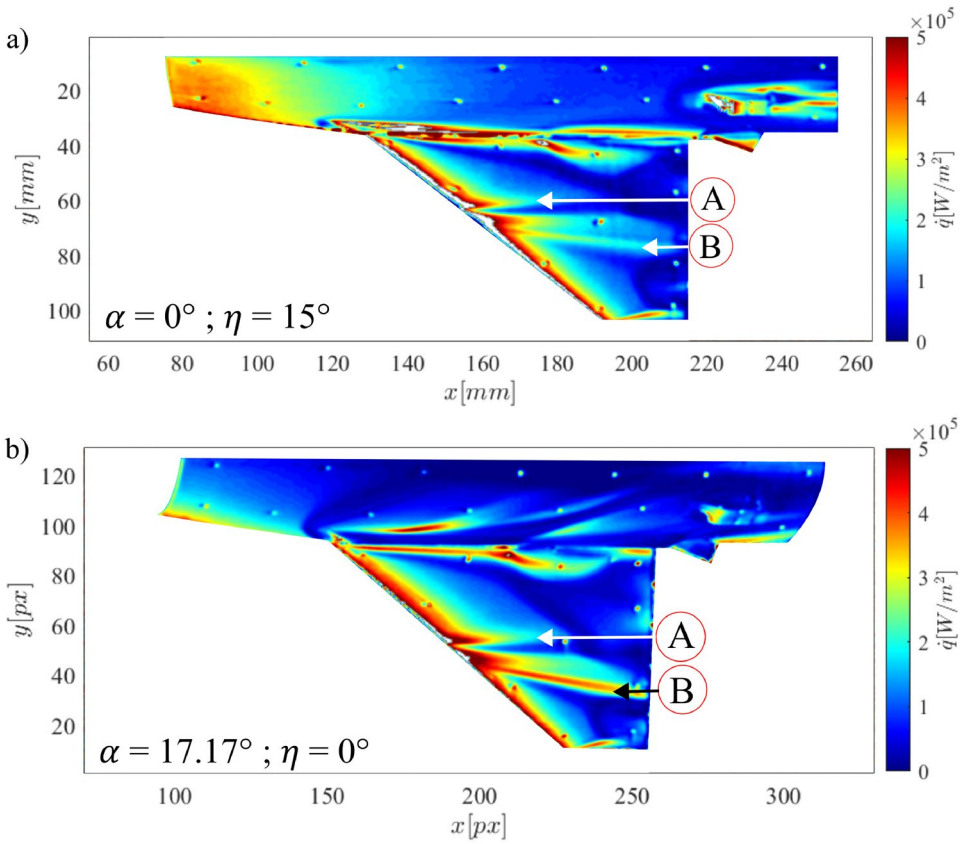

Fig. 18 Overview of the surface heat flux on the canard derived from TSP with different configurations of the forebody. **a** Model AoA $\alpha = 0° \pm 0.01°$, canard angle $\eta = 15° \pm 0.01°$; **b** model AoA $\alpha = 17.17° \pm 0.01°$, canard angle $\eta = 0° \pm 0.01°$. The canard angle (η) is defined relative to the body angle (α). Freestream flow is from left to right

the flow is expanding over the canard upper surface. This results in a limitation of the regions of high heating due to the shock–shock interaction at the canard, as compared with Fig. 14c, for example. The reattachment vortex is marked B and appears differently based on model angle of attack. In Fig. 18a, the vortex B undergoes a gradual reduction in heat flux in the streamwise direction However, in Fig. 18b, the vortex B creates a large and persistent surface heating due to the stronger bow shock generated by the model with a considerably larger angle of attack ($\alpha = 17.17°$).

These points were qualitatively matched in the RANS CFD solutions shown in Fig. 19. For the case with a model angle $\alpha = 0°$ and canard angle $\eta = 15°$ (Fig. 19a), the surface heat flux created by the vortex B reduces slightly in the streamwise direction but is lower than that measured in HEG. This streamwise surface heat flux remains approximately constant for the case with a model angle $\alpha = 17.17°$ and canard angle $\eta = 0°$ (Fig. 19c), qualitatively consistent with the experimental observations from Fig. 18b. The lower side of the canards, i.e. the windward sides, display considerably larger surface heat fluxes, as shown in Fig. 19b, d, wherein the colour scales have been broadened in their range for clarity. These higher surface heat fluxes

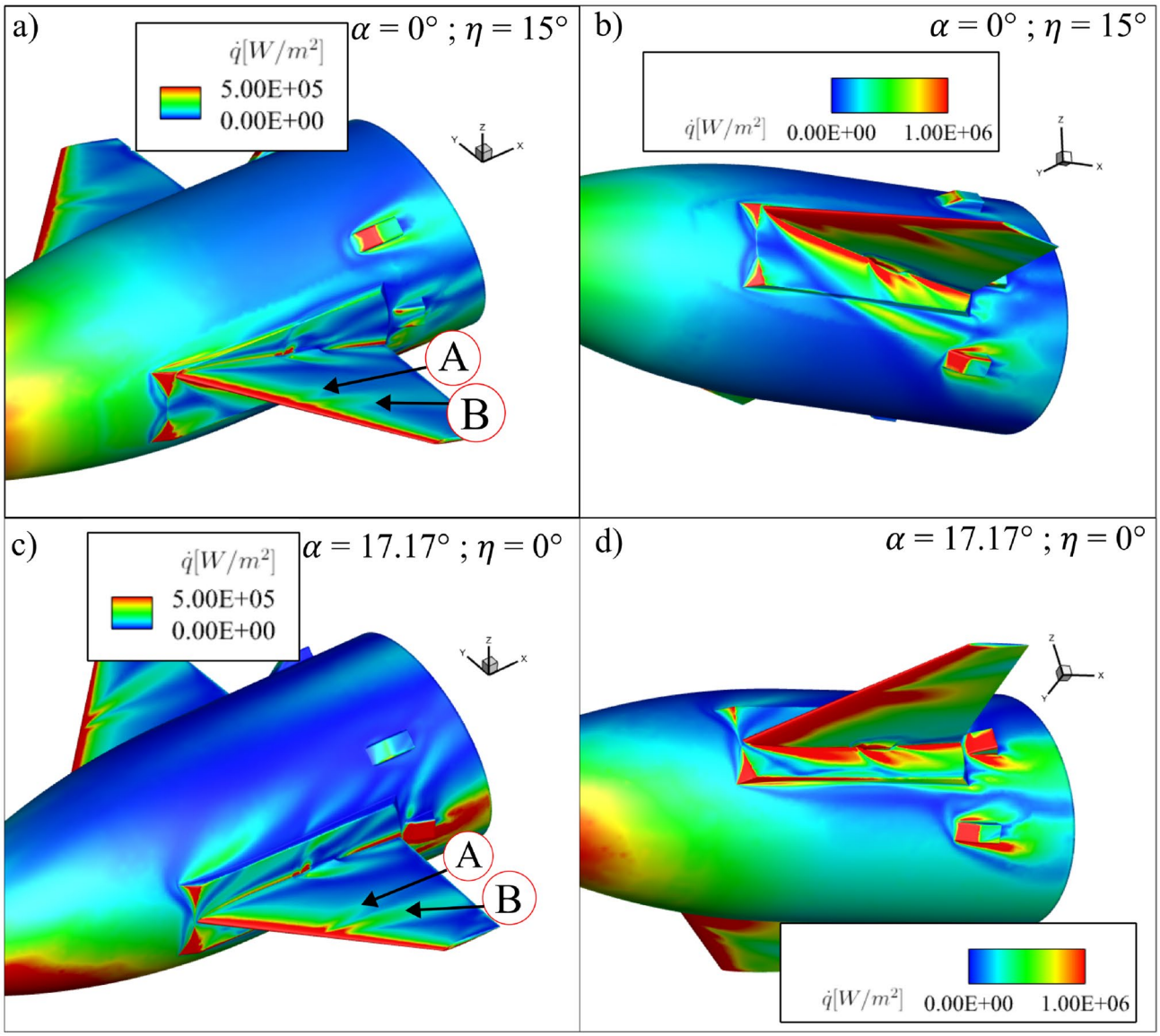

Fig. 19 Overview of the surface heat flux on the canard with different configurations of the forebody. **a**, **c** Model AoA $\alpha = 0° \pm 0.01°$, canard angle $\eta = 15° \pm 0.01°$; **b**, **d** underside of the model with AoA $\alpha = 17.17° \pm 0.01°$, canard angle $\eta = 0° \pm 0.01°$. The canard angle (η) is defined relative to the body angle (α). Due to large heating of the canard underside, the colour scales of **b**, **d** were broadened accordingly

are due to the additional compression of the flow along the lower side of the canard.

5 Effect of belly-up and -down configurations on shock–shock interaction at the canard

The return phase of the ReFEx payload is to involve a roll manoeuvre at angles of attack. This means that the payload geometry is to be configured with positive (belly-up) and negative (belly-down) body angles of attack. The effect of these configurations on the shock–shock interaction at the canard is discussed in this section.

For the cases presented in this section, the pixel values on an area of the canard windward surface are generally thresholded and blanked out (coloured white) due to saturated TSP signals from these pixels. Furthermore, temperature contours are shown for all cases discussed in this section as the calculation of heat flux resulted in large areas of thresholded pixels. Therefore, the interpretation given here is restricted to a qualitative one based on mean temperature fields extracted from the TSP images.

An overview of the thermal loading on the payload in the belly-down configuration is shown in Fig. 20. The thresholded pixels are coloured white in this figure. The region of large temperatures (and therefore high surface heat flux) occurs in the vicinity of the impingement of the leading edge shock on the canard, as discussed for previous cases. This is indicated by A in the figure. The development of a vortex along the canard is shown indicated by C. The outboard turning of this vortex is evident in this case, but reduced compared to the case with $\alpha = 0°$, and $\eta = 0°$.

During the roll manoeuvre and the transition from belly-down to belly-up configurations, the canards will be deflected for aerodynamic control purposes. The examination of a deflected canard relative to the body angle is based on results shown in Fig. 21a, b. For these tests, the model was configured with the same angle-of-attack magnitude and the canards were accordingly deflected such that the both

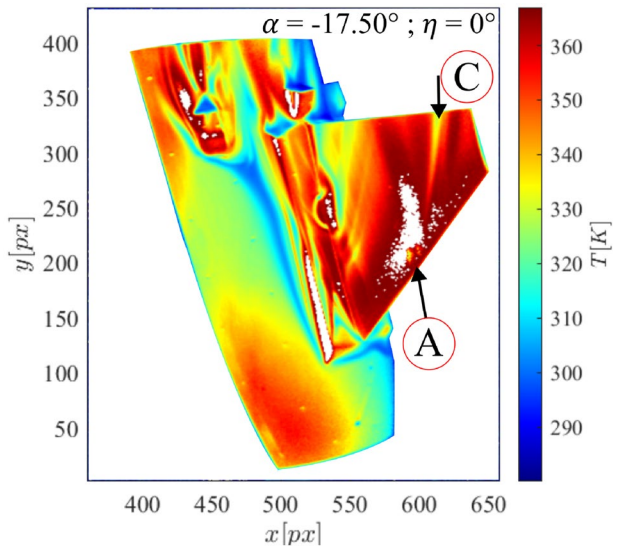

Fig. 20 Overview of the thermal loading on the payload in the belly-down configuration. Model AoA $\alpha = -17.50° \pm 0.01°$, canard angle $\eta = 0° \pm 0.01°$; Due to large heating of the canard windward surface, the absolute temperature contours are shown

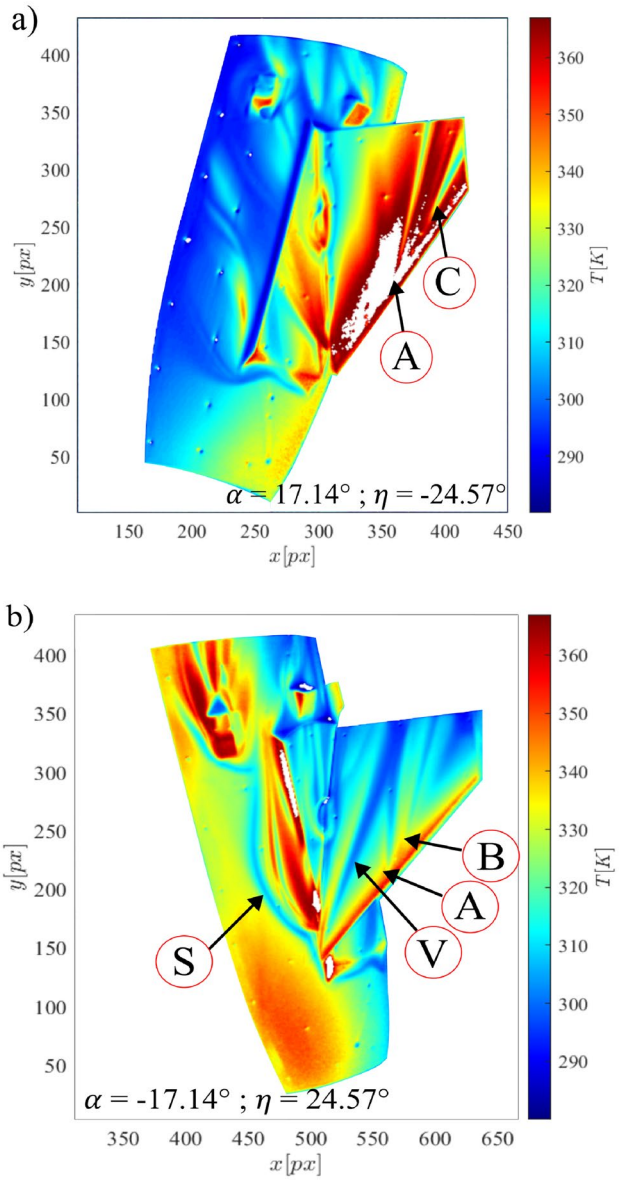

Fig. 21 Overview of the thermal loading on the payload in the belly-down configuration. **a** Model AoA $\alpha = 17.14° \pm 0.01°$, canard angle $\eta = -24.57° \pm 0.01°$; **b** model AoA $\alpha = -17.14° \pm 0.01°$, canard angle $\eta = 24.57° \pm 0.01°$. Due to large heating of the canard windward surface, the absolute temperature contours are shown

tests represent the same aerodynamic state of the model. This means that Fig. 21a shows the top view of the payload and Fig. 21b shows the bottom view. The canards were deflected towards the windward side of the body.

The large deflection of the canards meant that a larger portion of pixels on the canard windward surface had to be thresholded. However, the location of the leading edge shock impingement with the canard leading edge shock can nevertheless be approximated as indicated by the label A in Fig. 21a. The canard outboard vortex is shown by C and it is expected that reattachment of the boundary layer occurs at a location between A and C. The stronger shock interaction of this case results in a significant portion of the windward side of the canard being subject to large thermal loading, and would constitute a critical case for the ReFEx payload in the same configuration at its maximum flight Mach number of 5.

For the case shown in Fig. 21b, the leeside of the canard displays multiple vortices, the most persistent of which is labelled V, originating from the inboard leading edge and persisting until the trailing edge. Here, the shock–shock interaction at the canard is marked A, although the temperature contours indicate that the region of high heat flux would be limited in the streamwise spatial extent, as discussed for previous cases when examining the leeside of the deflected canard. Reattachment on the canard is indicated by B and high surface heat flux in this region is also limited in its spatial extent. Furthermore, the large deflection of the canard results in its shock wave impinging on the body of the payload, such that a separation vortex (labelled S) is evident in Fig. 21b. Reattachment and the resulting surface heating from the shockwave/boundary layer interaction occurring on the body of the payload model is evident towards the inboard edge of the canard to the right of the separation vortex S.

6 Conclusion and outlook

An assessment of surface heat flux on a 1:4 scale model of the ReFEx payload geometry has been carried out in the High Enthalpy Shock Tunnel Göttingen (HEG). Surface heat flux was assessed with the use of temperature sensitive paint (TSP) applied on the forebody and on a canard. Qualitative agreement was found to exist between RANS CFD simulations carried out at the same conditions as the experiments. Multiple flow features around the canard and its mounting structure were captured by the simulations. From the experiments, an extreme heat flux on the leading edge of the canard resulted in a localised loss of signal from the TSP in these regions. Regarding the RANS CFD, under the constraint of a laminar boundary layer at all locations on the geometry, the high surface heat loads measured in the experiments were not quantitatively reproduced by the CFD results. This was examined in detail regarding the shock–shock interaction at the canard, involving the nose bow shock and the canard leading edge shock. The transition to turbulence and the complex separation and reattachment phenomena presents a difficulty for RANS simulations to fully predict certain regions of local heating in the context of these complex phenomena. The Spalart–Allmaras turbulence model was shown to be promising in providing a better qualitative match with experimental data, in particular regarding regions of non-localised surface heating. It is important to note these limitations for the ReFEx geometry for possible uncertainty reduction in post-flight numerical analyses. Qualitative comparisons were favourable and conclusions on spatial locations of regions with high surface heating agree with the experimental measurements. The aspect of transition near the leading edge of the canard is still to be addressed and is planned for future work.

Acknowledgements The authors wish to thank the technical staff at HEG, in particular Leni Schmidt, Fabian Glasewald, Julian Ammer, Ingo Schwendtke and Uwe Frenzel for their extensive preparations of the HEG and instrumentation of the test model.

Author Contributions All authors contributed to the study conception and design. Experiments were performed by Divek Surujhlal and Alexander Wagner, data collection and analysis were performed by Divek Surujhlal and Viola Wartemann. The first draft of the manuscript was written by Divek Surujhlal and Viola Wartemann and all authors commented on previous versions of the manuscript. All authors read and approved the final manuscript.

Funding Open Access funding enabled and organized by Projekt DEAL.

Data availability statement Certain data discussed in this paper can be made available upon reasonable request.

Declarations

Conflict of interest The authors have no relevant financial or non-financial interests to disclose.

References

1. Rickmers, P., Bauer, W., Sippel, M., Stappert, S.: ReFEx: Reusability flight experiment—a flight experiment to demonstrate controlled aerodynamic flight from hypersonic to subsonic velocities with a winged RLV. In: 7th European Conference for Aeronautics

and Space Sciences (EUCASS). Proceedings of the 7th European Conference for Aeronautics and Space Sciences. Milan, Italy, 3–6 July 2017
2. Stappert, S., Rickmers, P., Bauer, W., Sippel, M.: Mission analysis and preliminary re-entry trajectory design of the DLR reusability flight experiment ReFEx. In: 8th European Conference for Aeronautics and Space Sciences (EUCASS). Proceedings of the 8th European Conference for Aeronautics and Space Sciences. Madrid, Spain, 1–4 July 2019. https://doi.org/10.13009/EUCASS2019-436
3. Bauer, W., Rickmers, P., Kallenbach, A., Stappert, S., Wartemann, V., Hans-Joachim Merrem, C., Schwarz, R., Sagliano, M., Grundmann, J.T., Flock, A., Thiele, T., Kiehn, D., Bierig, A., Windelberg, J., Ksenik, E., Bruns, T., Ruhe, T., Elsäßer, H.: DLR reusability flight experiment ReFEx. Acta Astron. **168**, 57–68 (2020). https://doi.org/10.1016/j.actaastro.2019.11.034
4. Rickmers, P., Bauer, W., Stappert, S., Kiehn, D., Sippel, M.: Current status of the DLR reusability flight experiment—ReFEx. In: HiSST: International Conference on High-Speed Vehicle Science and Technology, Moscow, Russia, 26–29 November 2018. https://doi.org/10.13009/EUCASS2019-436
5. Deutsches Zentrum für Luft - und Raumfahrt (DLR): The High Enthalpy Shock Tunnel Göttingen of the German Aerospace Center (DLR). J. Large-Scale Res. Facil. (2018). https://doi.org/10.17815/jlsrf-4-168
6. Schramm, J.M., Hannemann, K., Ozawa, H., Beck, W., Klein, C.: Development of temperature sensitive paints in the High Enthalpy Shock Tunnel Göttingen, HEG. In: 8th European Symposium on Aerothermodynamics for Space Vehicles, 2–6 March, Lisbon, Portugal, pp. 1–7 (2015). https://elib.dlr.de/93566/
7. Ozawa, H., Laurence, S.J., Schramm, J.M., Wagner, A., Hannemann, K.: Fast response temperature sensitive paint measurements on a hypersonic transition cone. Exp. Fluids **56**, 1853 (2014). https://doi.org/10.1007/s00348-014-1853-y
8. Schramm, J.M., Edzards, F., Hannemann, K.: Calibration of fast-response temperature sensitive paints for their application in hypersonic high enthalpy flows. In: Notes on Numerical Fluid Mechanics and Multidisciplinary Design XI, pp. 141–151. Springer. https://doi.org/10.1007/978-3-319-64519-3_13
9. Schramm, J.M., Hilfer, M.: Time response calibration of ultra-fast temperature sensitive paints for the application in high temperature hypersonic flows. In: Notes on Numerical Fluid Mechanics and Multidisciplinary Design XII, pp. 143–152. Springer.https://doi.org/10.1007/978-3-030-25253-3_14
10. Schramm, J.M., Schmidt, L.: Internal application of ultra-fast temperature sensitive paint to hydrogen combustion flow. In: Notes on Numerical Fluid Mechanics and Multidisciplinary Design XIII, pp. 121–131. Springer International Publishing.https://doi.org/10.1007/978-3-030-79561-0_12
11. Ecker, T., Schramm, J.M., Schmidt, L., Surujhlal, D., Wagner, A.: Shockwave boundary layer interaction of laminar/transitional flowpast a sharp fin. In: HiSST: 2nd International Conference on High-Speed Vehicle Science and Technology. Council of European Aerospace Societies (CEAS), 20–24 April, Bruges, Belgium (2020). https://elib.dlr.de/188440/
12. Cook, W.J.J.C., Felderman, E.J.: Reduction of data from thin-film heat-transfer gages—a concise numerical technique. AIAA J. **4**(3), 561–562 (1966). https://doi.org/10.2514/3.3486
13. Gerhold, T., Galle, O.F.M.: Calculation of complex three-dimensional configurations employing the DLR Tau-code. In: 35th Aerospace Sciences Meeting and Exhibit (1997). https://doi.org/10.2514/6.1997-167
14. Melber, S., Rudnik, A.R.R.: Structured and unstructured numerical simulation in high-lift aerodynamics. In: Workshop on European-Research on Aerodynamic Engine/Airframe Integration for Transport Aircraft, 26–27 September, Braunschweig, Germany (2000)
15. Schwamborn, D., Gerhold, T., Heinrich, R.: The DLR TAU-code: recent applications in research and industry. In: ECCOMAS CFD 2006 Conference. European Community on Computational Methods in Applied Sciences (ECCOMAS), 4–9 September, Netherlands (2006). Available on CD. https://elib.dlr.de/22421/
16. Reimann, B., Hannemann, V.: Numerical investigation of double-cone and cylinder experiments in high enthalpy flows using the DLR TAU code. In: 48th AIAA Aerospace Sciences Meeting Including the New Horizons Forum and Aerospace Exposition (2010). https://doi.org/10.2514/6.2010-1282
17. Mack, A., Hannemann, V.: Validation of the unstructured DLR-TAU-code for hypersonic flows. In: 32nd AIAA Fluid Dynamics Conference and Exhibit, 24–26 June, St. Louis, Missouri (2002). https://doi.org/10.2514/6.2002-3111. Paper ID: AIAA 2002-3111, eISBN: 978-1-62410-113-7
18. Pope, S.B.: Turbulent Flows. Cambridge University Press, Cambridge (2000). (**ISBN 978-1-316-17947-5**)
19. Jack, S., Oschwald, M., Eggers, T.: Mechanisms contributing to the dynamic stability of a flexible subscale rocket nozzle. J. Propuls. Power (2023). https://doi.org/10.2514/1.B39178
20. Wartemann, V., Konosidou, A.F.N., Merrem, C.: Comparison of CFD simulations and TMK wind tunnel data for the DLR ReFEx flight experiment. Notes Numer. Fluid Mech. Multidiscip. Des. (2021). https://doi.org/10.1007/978-3-030-79561-0_14
21. Spalart, P., Allmaras, S.: A one-equation turbulence model for aerodynamic flows. In: 30th Aerospace Sciences Meeting and Exhibit (1992). https://doi.org/10.2514/6.1992-439
22. Wagner, A., Schramm, J.M., Hannemann, K., Whitside, R., Hickey, J.-P.: Hypersonic shock wave boundary layer interaction studies on a flat plate at elevated surface temperature. In: Shock Wave Interactions, pp. 231–243 (2018). https://doi.org/10.1007/978-3-319-73180-3_19
23. Sandham, N.D., Schülein, E., Wagner, A., Willems, S., Steelant, J.: Transitional shock-wave/boundary-layer interactions in hypersonic flow. J. Fluid Mech. **752**, 349–382 (2014). https://doi.org/10.1017/jfm.2014.333
24. Schülein, E.: Skin friction and heat flux measurements in shock/boundary layer interaction flows. AIAA J. **44**(8), 1732–1741 (2006). https://doi.org/10.2514/1.15110